PAPER

Check for updates

Yellow emissive and high fluorescence quantum yield carbon dots from perylene-3,4,9,10-tetracarboxylic dianhydride for anticounterfeiting applications†

Namratha Ullal,[a] Bibekananda Sahoo,[b] Dhanya Sunil, [ID] *[a] Suresh D. Kulkarni, [ID] [c] Udaya Bhat K.[b] and Anand P. J.[d]

Forged products are widespread in the market and there is an immediate need to counter this growing menace. Anti-counterfeit techniques using fluorescent materials with covert features that appear hidden under daylight and display characteristic fluorescence upon specific source irradiation have gained popularity. Carbon dots (CDs) that can be prepared through facile synthesis from various raw materials are a class of fluorescent materials that provide tremendous opportunities to combat counterfeiting. This work focuses on the fabrication of perylene-3,4,9,10-tetracarboxylic dianhydride (PTCDA) derived CDs *via* the solvothermal approach and their subsequent purification using column chromatography. The fifth fraction obtained exhibited remarkable yellow emission (λ_{em} = 540 nm) with a high fluorescence quantum yield of 53.22% and a lifetime of 4 ns. The CDs appeared quasi-spherical during TEM imaging with an average diameter of 1–3 nm and appeared polycrystalline from the SAED pattern. The XPS and TEM-EDS results suggested carbon as the major element along with oxygen and nitrogen as the other heteroatoms. The water-based ecofriendly ink formulated using the CDs was printed on UV dull paper using the flexography technique. The print-proof paper samples appeared pale pink under daylight and fluorescent yellow upon 365 nm UV illumination. Moreover, the stability of the print was confirmed upon exposure to strong UV radiation cycles and abrasion resistance. Besides, the fluorescence emission remained unaltered even after 5 months of storage under room temperature conditions. The ink was used to print on PVC sheets and FBB boards with good stability against scuffing, suggesting its applicability in the packaging industry. The CDs could also serve as fluorescent markers for identifying post-consumer plastic packaging for a circular economy.

[a]*Department of Chemistry, Manipal Institute of Technology, Manipal Academy of Higher Education, Manipal 576104, Karnataka, India.*
E-mail: dhanyadss3@gmail.com, dhanya.s@manipal.edu
[b]*Department of Metallurgical and Materials Engineering, National Institute of Technology, Surathkal 575025, Karnataka, India*
[c]*Centre of Applied Nanosciences, Department of Atomic and Molecular Physics, Manipal Academy of Higher Education, Manipal 576104, Karnataka, India*
[d]*Manipal Technologies Limited, Manipal 576104, Karnataka, India*
†Electronic supplementary information (ESI) available. See DOI: https://doi.org/10.1039/d4dt02219j

1. Introduction

Carbon dots (CDs) that are zero-dimensional carbonaceous materials with sp[2] hybridized carbonaceous cores and sp[3] hybridized surface functional groups have gained wide popularity mainly due to their facile synthesis from inexpensive precursors, biocompatibility, and less toxicity.[1–5] As these carbonaceous nanoparticles have attractive emission features, they find applications in bioimaging,[6,7] bio-labeling,[8] metal-ion sensing,[9,10] drug delivery,[11,12] light emitting diodes,[13] photocatalysis and optoelectronic devices.[14–16] The bottom-up approach is the most used technique for preparing CDs with reduced surface defects,[17,18] and the use of precursors rich in carbon (C), nitrogen (N), oxygen (O) and sulphur (S) can facilitate the fabrication of CDs with enhanced fluorescence behavior.[19,20] A plethora of reports describe different fabrication routes for CDs with diverse chemical groups and thereby unique luminescence features from synthetic molecules, food items, plant and animal biomass, and waste materials.[21–25] Though nanoparticles obtained through the top-down method exhibit higher crystallinity and superior fluorescence attributes compared to bottom-up approaches, these techniques are less frequently employed due to not only harsh reaction conditions and chemical environment, but also sophisticated and expensive techniques that add to high cost during large-scale production. Among the bottom-up methods, the hydrothermal/

solvothermal approach is extensively employed due to its scalable and simpler process and is considered as one of the softer approaches for preparing highly fluorescent CDs.[26–30]

There are a few studies that report dyes as source materials for the preparation of CDs. Zheng *et al.* synthesized NIR emissive CDs from a hydrophobic cyanine dye *via* the solvothermal approach for NIR fluorescence imaging and *in vitro* photothermal therapy.[31] Gao *et al.* were successful in the fabrication of highly coveted red emissive CDs using the neutral red dye *via* a hydrothermal method with the application extended to metal ion sensing and bio-imaging without any background fluorescence interference.[32] Li *et al.* attempted to prepare blue, green, yellow, and red dye-based CDs *via* solvent engineering, and these multi-color nanomaterials were used in polyvinyl alcohol (PVA) composite films and LED fabrication.[33] However, most of these dye-derived carbonaceous nanodots exhibited lower quantum yields (QYs) when used as such without any further purification processes. The byproducts generated during their synthesis can significantly contribute and influence the fluorescence associated with CDs, which needs to be eliminated to achieve error-free results for real-life utility of these nanomaterials. CDs with desirable fluorescence properties including narrow and longer wavelength emission, high quantum yield, a long fluorescence lifetime and good photostability have versatile practical applications and are always in demand. The significance of purification, specifically for luminescence-based characterization studies, is highly critical and imperative.

Perylene-based polycyclic aromatic dyes have been implemented in many technological fields due to their outstanding physical and optical properties as well as their propensity towards self-assembly.[34] As they possess captivating optical and thermal stabilities as well as chemical inertness, they are utilized in solar cells, light-emitting diodes, thin film transistors and bioimaging. There are a few studies reported on the synthesis of CDs from perylene dyes for CO_2 sensing and cell imaging.[35] Wang and group synthesized CDs using PTCDA and polyethyleneimine *via* a hydrothermal method. As opposed to the hydrophobic nature of precursors, the as-prepared CDs could be dispersed in water, which displayed a QY (by the absolute method) of 0.058. Additionally, these CDs were utilized for the anti-bacterial effect on common Gram-positive pathogens.[35] Another research group reported the synthesis of greenish-yellow emissive CDs by a hydrothermal approach with an estimated QY of 26.6%. They exhibited solvatochromism and long-term photostability and were utilized in multi-colour cellular bioimaging.[36] Different approaches need to be explored for avoiding aggregation-induced quenching in solid state applications and improving the fluorescence QY of CDs.

In this work, we chose PTCDA as the precursor due to its extensive conjugated structure. A solvothermal approach was employed to obtain stable yellow emissive CDs. Furthermore, the photophysical properties of pure CDs were investigated. Furthermore, an ink formulation was developed by suspending the CDs in PVA and printed on UV dull paper and packaging substrates *via* the flexography technique. The print proofs exhibited good photostability even after 5 months of storage, indicating their inertness under ambient conditions. The printed samples were studied for use in anti-counterfeiting and packaging applications.

2. Experimental

2.1. Synthesis and characterization of CDs

About 50 mg of PTCDA in 7 mL *N*-methyl-2-pyrrolidone (NMP) and 1 mL ethanol was taken in a Teflon coated autoclave (25 mL capacity). The reaction setup was fixed at 155 °C for 1, 3 and 5 h durations, and the resultant mother liquor (ML) was filtered to separate the suspended solids. Silica gel (400–700 meshwork; SRL Chemicals) was used to achieve wet packing for column chromatography.

UV–visible spectra were recorded from 200–800 nm at a scan rate of 4800 nm min^{-1} in a 1cm dimension quartz cuvette (1.0 nm bandwidth) using an 1800 Shimadzu UV–visible spectrophotometer. Fluorescence measurements were obtained using a JASCO spectrofluorometer FP-8300 with a path length of 10 mm and varying excitation and emission bandwidths between 2.5 to 5 nm. QY measurements were performed for excitation and emission bandwidths between 2.5 and 5 nm using the absolute method where an integrating sphere coated with $BaSO_4$ was attached to the PL instrument. The LC-MS data were collected using an ACQUITY UPLC H-Class PLUS Bio System. The sample was injected into a C18 LC column with a mesh size of 1.7 μm. The binary elution system chosen was water + 0.1% formic acid and methanol. The separated fractions were analysed through positive electrospray ionisation time-of-flight mass spectrometry. The ATR-IR data with 40 scans of 4 cm^{-1} resolution were acquired using a Shimadzu-IR Spirit instrument. X-ray diffraction patterns were collected for 2θ extending from 10 to 80° on a Malvern PANalytical, Empyrean 3rd Gen instrument with a Cu Kα source. The XPS data were obtained for 10 min with spectral scan from 63.6 to 1253.6 eV using an Omicron XPS system with non-monochromatic Mg-Kα and Al-Kα excitation sources. The Raman spectrum was acquired using a Renishaw Compact Raman spectrometer in a continuous scan mode operation with 10 s exposure time and the wavelength of the excitation source corresponded to 785 nm with 0.05% power. The surface charge of the CDs was estimated using a Malvern Panalytical – Zetasizer Ver. 7.12 instrument. TEM images were acquired using a JEM 2100 F model equipment with a 200 kV electron source. About 10 μL of CDs in 1 mL methanol dropcast and dried under ambient conditions on a 200 mesh carbon coated copper grid was used for TEM analysis. A Talos F200 S model instrument was employed for SAED, TEM-EDS and elemental mapping and Image-J software was used to analyse the images. A DeltaFlex TCSPC lifetime fluorimeter equipped with a Mai Tai laser (λ_{ex} = 340–510 nm) as a short-pulse oscillator and HPPD with conventional PMT design was used to record the fluorescence lifetime data.

2.2. Preparation of flexo-ink and study of print properties

Table 1 summarizes the formulation adopted for ink preparation using PTCDA-derived CDs for flexography printing.

Table 1 Composition of the ink formulation

Components	Composition (weight %)
Colorant concentrate (CD dispersion)	35.38
8% PVA	51.83
30% glycerol–ethanol mixture	12.23
Ammonia solution	0.56

The grammage (in gsm) of uncoated and coated UV dull paper used for printing the proofs was measured using a Digital GSM tester. The ink was coated on UV dull paper with a zero number K bar coater (wet film deposit = 4 mm). The flexo-prints were obtained using RK Flexiproof 100 at 50 m min⁻¹, 9.5 BCM Anilox roll, chambered doctor blade inking equipment, and a photopolymer plate. The density and colorimetric (L^*, a^*, and b^*) values of the printed paper samples were measured using an Xrite i1 Pro spectrophotometer. The rub resistance of the printed film was tested using a Sutherland ink rub tester by using a 2 lb weight for 50 and 100 rubs.

2.3. Preparation of PVA-CD films

About 9 g of PVA granules was added to 30 mL de-ionized water and heated at 90 °C to achieve complete dissolution. The solution was further cooled under ambient conditions to obtain 30% PVA solution. CDs (0.4, 0.8, 1.2, 1.6 and 2.0 mL in 7 : 3 methanol : dichloromethane (DCM)) were dispersed in 5 mL of viscous 30% PVA solution through sonication for 24 h under room temperature conditions. The resultant homogenous solution was poured into a petri-plate and dried at 100 °C under vacuum for 8 h. The PVA film without CDs was also prepared in a similar manner to the control.

3. Results and discussion

3.1. Synthesis of CDs

PTCDA with abundant oxygen atoms and low solubility in aromatic solvents was used as the precursor material for preparing the CDs. The stable organic molecule displays high molar absorptivity, excellent optical and thermal stability, reversible redox features, and self-assembly behaviors.[37] The 5-membered lactam NMP was used as a colorless, nonvolatile dipolar aprotic organic solvent, which is stable at room temperature. However, at elevated temperatures and in the presence of certain reagents (acids or alkali) it is susceptible to ring opening hydrolysis reactions.[38] Five absorbance peaks at 303, 460, 490 and 527 nm were noticeable in the precursor spectra (Fig. 1a). The solution of PTCDA in NMP and ethanol was subjected to a solvothermal reaction at 155 °C for 1, 3 and 5 hours as mentioned in the Synthesis and characterization of CDs section to obtain the respective ML-1, ML-3 and ML-5. The UV–visible spectra of a few aliquots of these three MLs were analysed and compared with that of the precursor. The absorption of all ML samples appears similar to that of the precursor, probably due to the possession of similar chemical groups.

3.2. Purification of CDs using column chromatography

Before carrying out large scale separation of MLs, thin layer chromatography (TLC) was performed for ML-1, ML-3 and ML-5 using different ratios of DCM–methanol solvent systems. Fig. S1a–c† depict the TLC separations for the three samples, respectively. Based on the separations observed on the TLC plate, the DCM : methanol elution system with the following ratios: 9 : 1, 7 : 3, 6 : 4 and 3 : 7 was chosen to ensure efficient separation of the ML samples.

Column chromatography is one of the efficient techniques to separate the products from redundant reactants and the byproducts generated. A few aliquots of the ML sample were
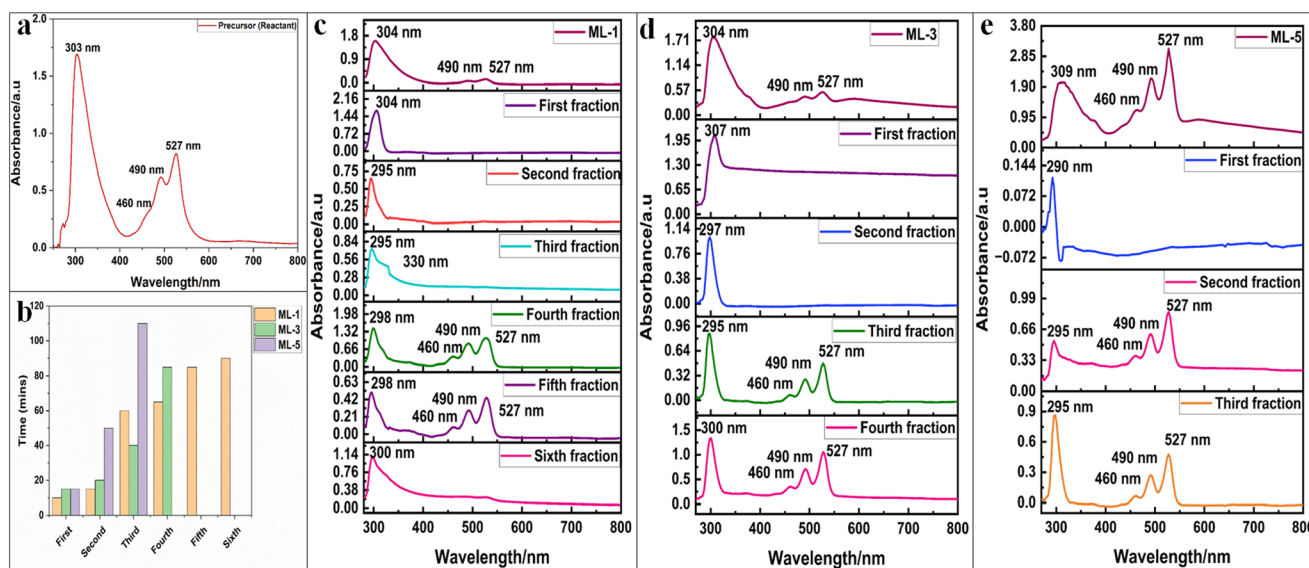

Fig. 1 (a) UV–Visible spectra of PTCDA in NMP. (b) Graphical representation for the retention time for different fractions corresponding to ML-1, 3 and 5 to elute from the column. UV–Visible spectra of purified fractions in comparison to the corresponding spectra of (c) ML-1 (d) ML-3 and (e) ML-5.

added to the top of the column and different elution systems with increasing polarity were allowed to run through the column. Fig. S2–4† depict the photographs of column chromatography separation of ML-1, ML-3 and ML-5 along with different fractions observed under daylight and UV illumination. On increasing the polarity of the solvent, gradually different fractions eluted from the column. Six, four and three fractions respectively were eluted based on the polarity differences for ML-1, ML-3, and ML-5. The purity of the fractions obtained was evaluated based on TLC observations, which displayed a single spot. The purified fractions corresponding to different reaction durations vary along with the time taken to exit the column. The number of fractions eluted decreased with increasing reaction duration. Fig. 1b pictorially portrays the retention time for different fractions corresponding to ML-1, ML-3 and ML-5 to elute from the column and Table S1† lists the retention time values. As no significant difference in absorbance wavelengths was noticed in the UV spectra of these three MLs, it can be assumed that a longer duration ensures fewer by-products. This assumption was confirmed during the column separation as only 3 fractions were obtained from ML-5 compared to 4 and 6 in the case of ML-1 and ML-3. Moreover, the retention time does not show a major difference and further substantiates that these eluted fractions of ML-1, 3 and 5 could have similar chemical behaviour.

3.3. Electronic spectral analysis of column-separated fractions of MLs

As discussed in the earlier section, the absorption bands of all the three MLs are analogous to that of the precursor PTCDA in NMP, irrespective of their absorption intensities. Post synthesis the ML samples retained the perylene group framework and similar chemical groups, irrespective of the reaction duration. Furthermore, the UV spectra of the different fractions recorded after column purification were compared with those of the respective MLs. As evident from Fig. 1c, the UV absorption peaks at 295–304 nm of all six fractions of ML-1 correspond to the NMP moiety. The peaks in the fourth and fifth fractions centred at 460, 490 and 527 nm were predominately observed in the precursor and ML-1.[39] All four fractions of ML-3 display bands at 295–307 nm due to the presence of the NMP moiety (Fig. 1d). In addition, the third and fourth fractions also display peaks at 460, 490 and 527 nm akin to ML-3 and precursor samples. Similar observations were found for the second and third fractions of ML-5 with absorption bands at 460, 490 and 527 nm (Fig. 1e). Thus, the latter fractions of all the three MLs exhibited similar absorptions as the precursor PTCDA.

Initially, the 3D photoluminescence spectrum of PTCDA in NMP was analysed to evaluate the changes observed in the ML samples after subjecting it to solvothermal treatment. The 3D spectrum (Fig. 2a) shows the major emission at 580 nm for excitations at 380 nm (marked as A) and 430 nm (marked as B). Accordingly, the 2D spectrum (Fig. 2b) depicts a minor emission at 632 nm for the same excitations (*i.e.*, 380 and 430 nm) in addition to the major emission at 580 nm. The ML samples corresponding to 1, 3 and 5 h display different emissive regions indicating the successful chemical changes after adopting a solvothermal approach. The 3D (Fig. 2c) and 2D
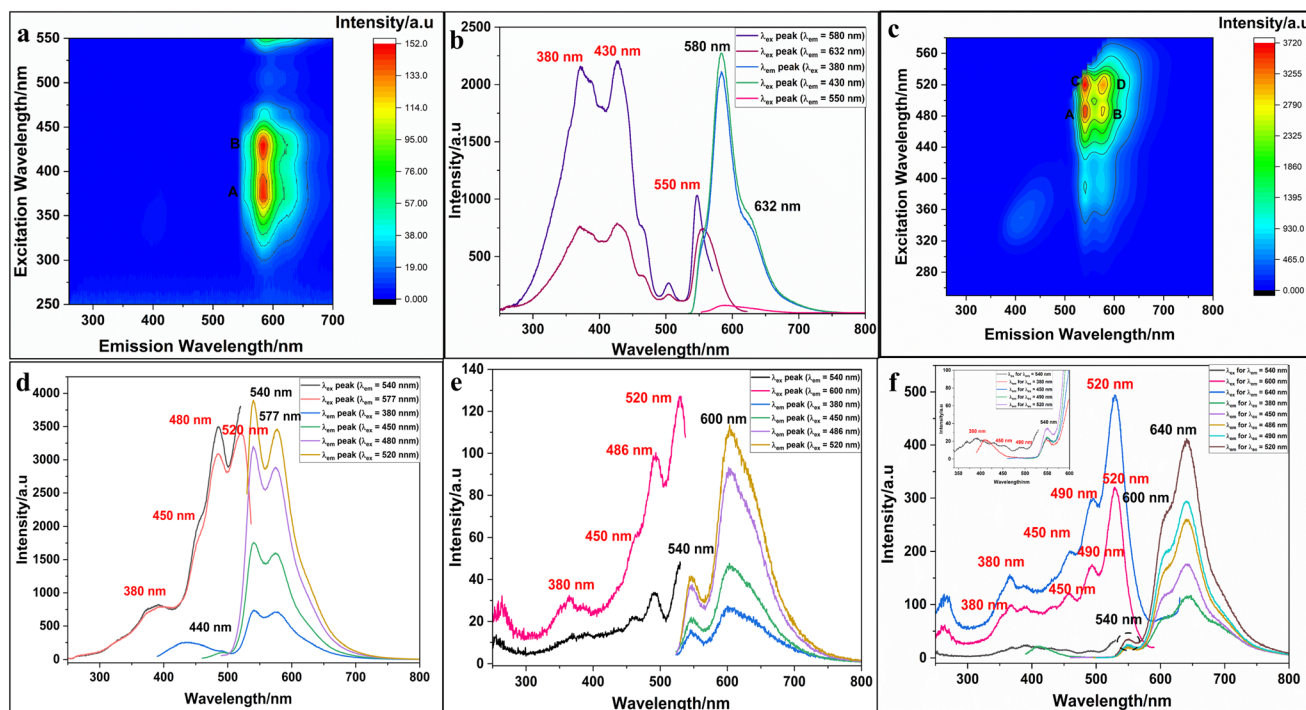

Fig. 2 (a) 3D and (b) 2D photoluminescence spectra of PTCDA; (c) 3D and (d) 2D photoluminescence spectra of ML-1. Photoluminescence spectra of (e) ML-3 and (f) ML-5.
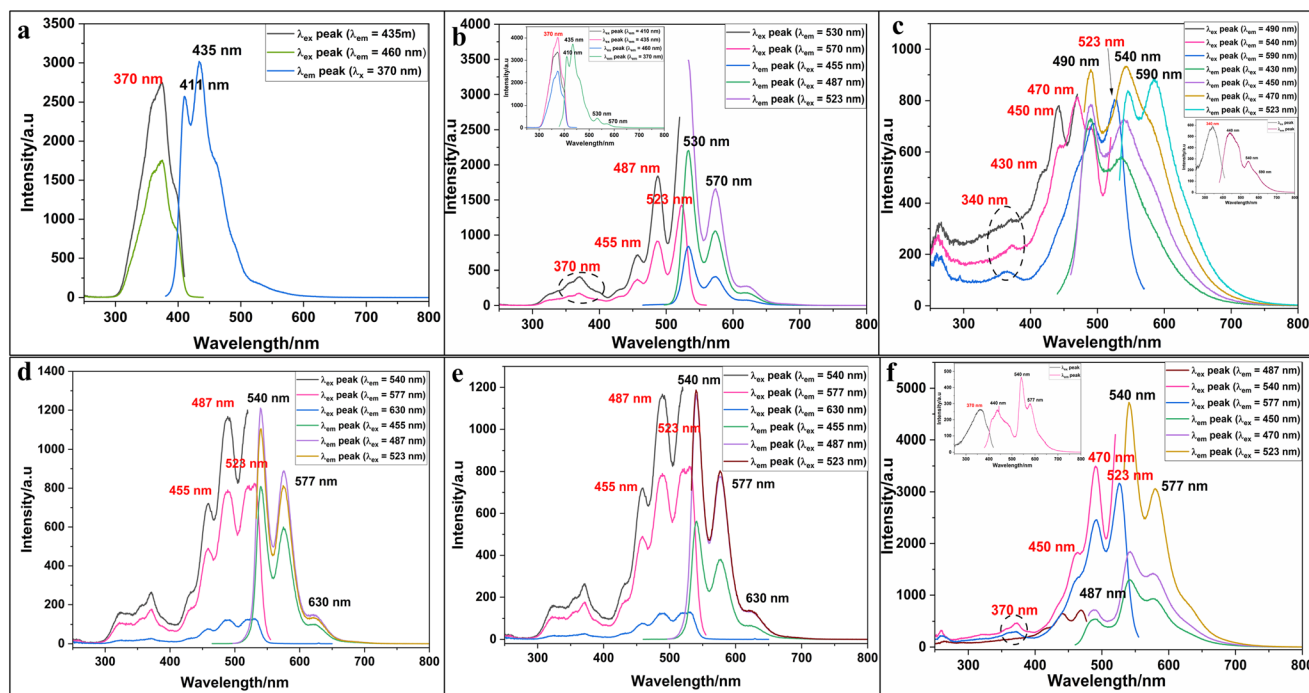
Fig. 3 Emission spectra of (a) first, (b) second, (c) third, (d) fourth, (e) fifth and (f) sixth fractions of ML-1.

spectra of ML-1 show emissions centred at 440, 540 (major emission) and 577 nm for excitation wavelengths corresponding to 380, 450, 480 and 520 nm (Fig. 2d). Interestingly, with prolonged duration of the solvothermal reaction, the emission intensity at 540 nm decreases significantly, which is evident in the 2D spectra of ML-3 and ML-5 samples exhibiting maximum emission at 600 and 640 nm respectively (Fig. 2e and f). Furthermore, to check the contribution of the solvent, the 3D spectrum (Fig. S5†) of NMP was also recorded, which exhibits a major emission at 412 nm (λ_{ex} = 350 nm) and a less intense emission at 532 nm (λ_{ex} = 380 nm).

The emission features of purified fractions corresponding to ML-1, ML-3 and ML-5 were also analysed. The six fractions that were eluted from ML-1 exhibited varying emissive properties. The first fraction (Fig. 3a) displayed major emissions at 411 and 435 nm, while the second fraction (Fig. 3b) exhibited emission at 530 nm. The third fraction (Fig. 3c) also showed similar peaks with intense emissions at 490, 540 and 590 nm. Moreover, the fourth and fifth fractions (Fig. 3d and e) exhibited emissions at 540, 577 and 630 nm. The sixth fraction (Fig. 3f) emitted majorly at 540 and 577 nm. The emission profiles of the latter three fractions are analogous to that of ML-1 indicating similar transitions.

The first fractions of ML-3 and ML-5 (Fig. S6a and S7a†) show peaks positioned at 407, 432–433 and 460 nm with less intense emissions extending towards higher wavelengths. The second fractions of both ML-3 and ML-5 (Fig. S6b and S7b†) exhibit emissions at around 533, 574 and 624 nm. The latter fractions of both ML-3 (Fig. S6c and d†) and ML-5 (Fig. S7c†) have predominant emissions at 540 nm with less intense emis-

sions at 577 and 632 nm. In general, the first and second fractions of all MLs of less polarity have major emissions corresponding to lower wavelengths, while more polar fractions have major emissions corresponding to the yellow region.

3.4. Mass spectral studies

Initially, it is imperative to understand the individual contribution of the precursor materials in fluorophore formation during the solvothermal reaction. The contribution of NMP towards the formation of fluorophores in the ML-1 sample was investigated using LC-MS. The chromatogram of the ML-1 sample was compared with that of the product obtained after the solvothermal reaction of NMP alone under the same conditions. The chromatogram of ML-1 (Fig. S8a†) indicates the presence of 11 peaks which were analysed for mass spectrometry (Fig. S8b†). The absence of a peak at m/z = 392.32 g mol^{-1} corresponding to the molecular weight of PTCDA suggests the absence of the precursor pigment in the solvothermal product, whereas the LC separations of the solvothermal product of NMP exhibited three fractions as shown in the chromatogram (Fig. S9a†). The mass spectra (Fig. S9b†) acquired for the three components showed peaks at m/z = 171.1 and 207.1 (Peak ID 1 & 2 in Fig. S9b†) and only 207.1 (Peak ID 3 in Fig. S9b†) suggesting the ring opening process in addition to polymerization and oxidation reactions of NMP during the solvothermal reaction.[38,40] Notably, the chromatogram of ML-1 also displayed peaks at similar m/z values of 171.1 (Peak ID 1 & 2 in Fig. S8b†) and 207.1 (Peak ID 10 in Fig. S8b†), indicating contributions from NMP.

3.5. Fluorescence QY and lifetime measurement studies

PTCDA and NMP precursors exhibited characteristic fluorescence. PTCDA showed emission at 580 nm (λ_{ex} = 380 nm), whereas NMP displayed maximum emission at 412 nm (λ_{ex} = 350 nm). The solvothermal product of NMP showed maximum emission at 530 nm (λ_{ex} = 440 nm) (Fig. S10†). Song and group have already investigated the fluorescence properties of compounds with pyrrolidone ring(s).[40] Compounds in the innate form exhibit weak fluorescence and on derivatization show strong fluorescence. PTCDA and NMP afforded absolute QYs of 3.76% and −2.60% respectively. However, ML-1 and the solvothermal product of NMP alone (1 h at 155 °C) exhibited QYs of 9.78% and 1.27%. It can be noted that NMP showed weak fluorescence with a very low QY, but post solvothermal treatment displayed green emission (λ_{em} = 530 nm) with a relatively increased QY.

As the reaction duration does not induce major changes in the emission region, fourth, fifth and sixth fractions of ML-1 were chosen for further analysis. Absorption of light (10^{-15} s) involves two non-radiative processes taking place simultaneously, namely (i) vibrational and (ii) solvent relaxation (10^{-12} s) followed by radiative fluorescence (10^{-9} s).[41] Steady state measurements are not sensitive to molecular dynamics associated with conformational changes. Time-resolved fluorescence (TRF) serves as an important tool to understand the formation of excitons (electron–hole pair) during radiative decay ($S_1 \rightarrow S_0$).[42] TRF was facilitated via the time correlated single photon count (TCSPC) technique equipped with a high repetition rate picosecond or femtosecond laser source. The conditions were adjusted such that less than one photon was detected per laser source.[42] Fluorescence lifetime refers to the time when a molecule remains in the excited state before reaching the ground state. Previous studies have reported CDs exhibiting multiple lifetime values with either bi- or triple-exponential decay, which are due to the presence of diverse chemical groups on the surface of CDs.[43] This leads to a more complicated de-excitation pathway leading to multiple lifetimes. There are a few reports that state the mono-exponential decay nature of CDs.[44,45] In our findings, we report the presence of mono-exponential decay observed in the fourth, fifth and sixth fractions due to the presence of single photoluminescence centres or emissive traps.[46] The lifetime plots were fitted using the mono-exponential function represented by $I_{(t)} = A \cdot e^{(-t/\tau)}$, where $I_{(t)}$ is the lifetime, A is the normalized amplitude and τ is the decay time constant. Tables S2–4† list the lifetime (τ_1) and pre-exponential factor (A_1) along with the average lifetime (τ_{avg}).[47] The fourth (Fig. S11a–c†) and fifth (Fig. 4a–c) fractions showed a lifetime value of 4.0 ns for different emitters. This can indicate that surface states of CDs mainly have a single emission centre, and excited electrons return to the ground state via a radiative transition.[46] Similar observations were recorded for the sixth fraction with constant lifetime values (Fig. S12a–c†) for different excitations. Lower lifetime values of 1.39 and 1.67 ns for emissions at 435 and 487 nm, respectively are observed for excitation at 370 nm. For emissions at 488 nm, the measured lifetime is 3.95 ns, whereas emissions at 540 and 580 nm (yellow and orange emission) have notably higher lifetime values of 4.35 and 4.34 ns. Therefore, for a single excitation, one species (487 nm) exhibits faster decay in comparison to a longer decay (540 and 580 nm) component.
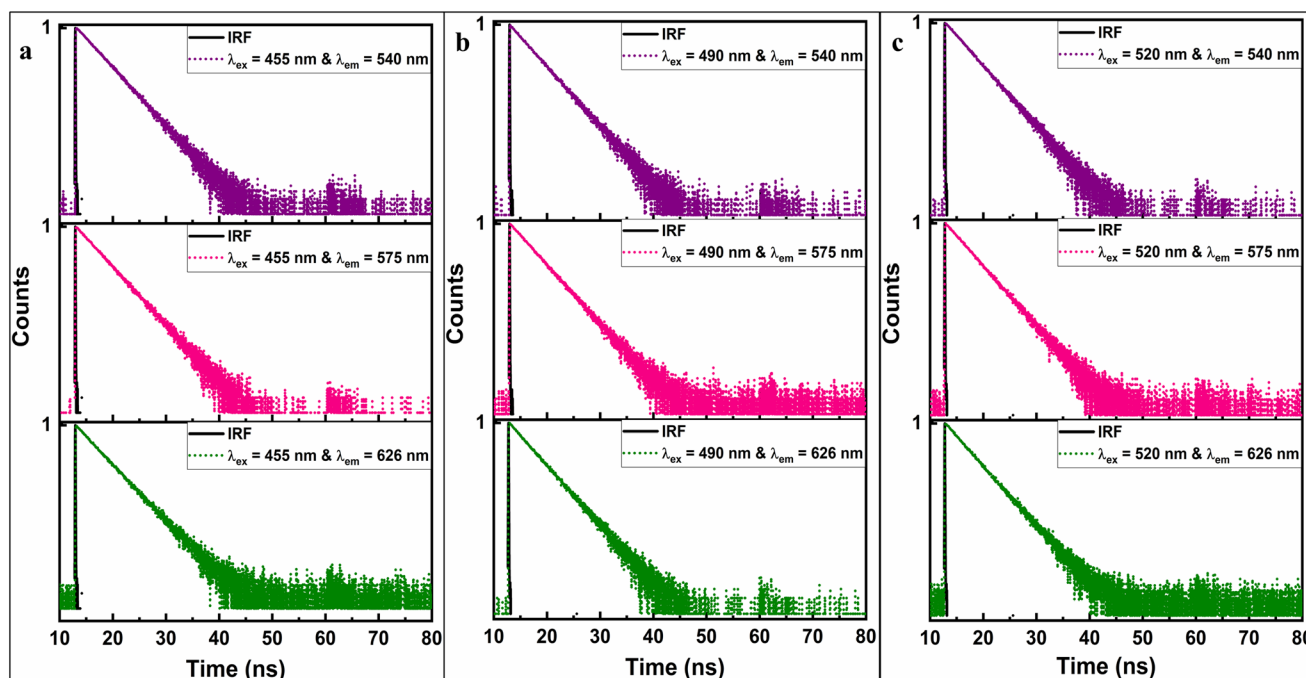

Fig. 4 Time-resolved fluorescence spectra of the fifth fraction recorded at (a) 455 nm, (b) 490 nm and (c) 520 nm with mono-exponential decay.

Post column chromatography separation, the fourth, fifth and sixth fractions exhibited QY values of 4.94, 53.22 and 43.76%, respectively as presented in Fig. S13.† The purification enabled separation of individual components which can show their actual photostability. Considering the estimated QY (ϕ_F) and average fluorescence lifetime (τ_f), the fluorescence rate constant (k_r) values of CDs were calculated ($k_f = \phi_F/\tau_f$).[48] A higher radiative rate constant is observed for the fifth fraction compared to the fourth and sixth fractions (Table S5†). The increase in radiative rate constant is highly desirable due to the increase in radiative centers because of stronger transitions.[49,50] The fifth fraction exhibited a considerably higher rate of radiative constant along with a higher QY and is hence chosen for further spectroscopic studies and formulation of security ink.

3.6. Structural and chemical studies

XRD analysis was performed to investigate the crystallinity of the sample. The XRD spectrum presents a broad peak centred at 22.1 along with other sharp peaks (Fig. 5a). The appearance of a broad peak can be due to the contribution from the glass slide (Fig. 5b). Notably the sharp peaks recorded are overlaid with graphite-2H as the standard reference. Table S6† lists the 2θ values and the respective diffraction planes for the reference sample. The peak at 26.3 belongs to the (002) plane of diffraction. However, the appearance of sharp peaks at 43.1 and 44.0 (marked as b & c in the reference) corresponds to the (100) and (101) plane of diffraction. In addition, the less intense peak at 50.2 overlaps with the peak (marked as d in the reference) belonging to the (102) plane of diffraction. A closer match of the XRD spectrum with the reference can infer the arrangement of lattice points akin to graphite carbon. In accordance with Bragg's equation, the d-space values of 26.3, 43.1 and

50.2 were estimated to be 0.34, 0.21 and 0.18 nm. Raman spectra were collected for the fifth fraction under 785 nm excitation (Fig. 5c). The Raman spectrum of the fifth fraction exhibits a prominent D-band and a less intense G-band at 1380 and 1607 cm^{-1}, respectively due to contributions from sp^3 and sp^2 hybridised carbon groups.[51] Raman spectra were also recorded for PTCDA and NMP. PTCDA exhibits a peak at 1054 cm^{-1}, which can be ascribed to the out-of-plane C–C–H deformation and two distinct peaks at 1310 and 1381 cm^{-1} correspond to in-plane C–H bending and C–H stretching vibrations. The presence of C=C in aromatic groups is evident from the peak at 1456 cm^{-1}. Moreover, the bands at 1576 and 1595 cm^{-1} appear due to the strong contribution of C–C in the perylene group. The anhydridic C=O in PTCDA appears as weak bands at 1776 and 1877 cm^{-1}.[52,53] NMP displays peaks at 622, 749 and 930 cm^{-1} corresponding to N–C–C bending, H–C–H bending and C–C–C symmetric stretching vibrations. In addition, the peaks at 1026, 1228, 1430 and 1670 cm^{-1} belong to out-of-plane C–C–H deformation, C–N stretching, –CH$_3$ bending and C=O stretching vibrations.[54] Thus, we can confirm that post synthesis, the fifth fraction possesses distinct distorted carbon groups (sp^3) and a perylene core (sp^2). In addition, a broad peak at 1894 cm^{-1} can be assigned to the C=O stretching vibration. Table S7† summarizes the Raman shift values for PTCDA, NMP and the fifth fraction acquired under 785 nm excitation.

Furthermore, ATR-IR spectra recorded for the fifth fraction are compared with PTCDA powder and NMP (Fig. 5d). The PTCDA spectrum presents numerous bands between 734–860 cm^{-1} attributed to out-of-plane and in-plane C–H bending vibrations. The peaks at 1017 and 1120 cm^{-1} are mainly due to C–H in-plane bending and –CO–O–CO–C stretching vibrations observed in the anhydride group.[55,56] The
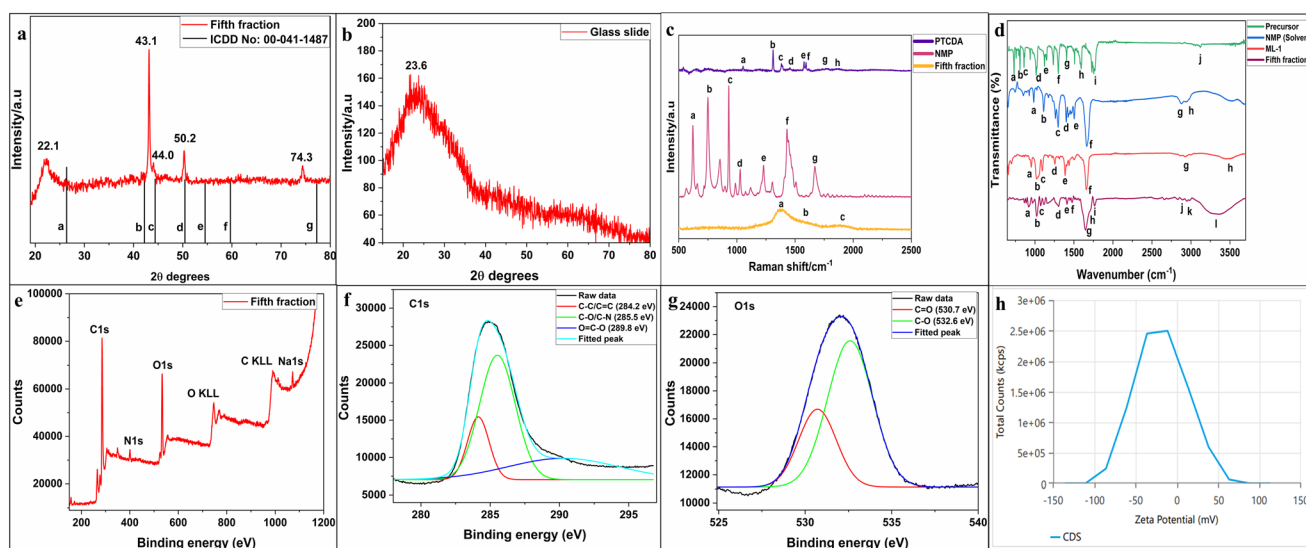

Fig. 5 XRD spectra of (a) fifth fraction and (b) glass substrate. (c) Raman spectra of PTCDA, NMP and the fifth fraction collected at 785 nm. (d) Overlaid FT-IR spectra. (e) XPS survey spectra and full scan spectra of (f) C 1s and (g) O 1s of the fifth fraction. (h) Zeta potential estimation of the fifth fraction.

C–O stretching peak is centred at 1300 cm^{-1}, whereas the occurrence of distinct signals for C=C of the perylene ring can be found at 1409–1594 cm^{-1}. The distinct C=O and =C–H group stretches are observed at 1764 and 3118 cm^{-1}. The absorption spectrum of NMP has characteristic peaks at 984 cm^{-1} ascribed to out of plane C–H bending vibrations. The peak for C–N stretching vibrations is found at 1295 cm^{-1}. In addition, the peaks at 1398 and 1505 cm^{-1} correspond to CH$_3$ and CH$_2$ bending vibrations and the amide C=O bond appears at 1665 cm^{-1}. The C–H symmetric and asymmetric stretches are observed at 2875 and 2957 cm^{-1} in the spectra.[54,57] ML-1 and the fifth fraction display various absorbance peaks for C–H, C–O, C–N and C=O vibrations like the precursor and NMP. The ML obtained after solvothermal synthesis exhibits a peak at 1660 cm^{-1} due to the presence of NMP. Post column purification of the ML sample, the fifth fraction exhibits peaks at 1650 and 1764 cm^{-1} corresponding to C=O of amide and anhydride as observed in NMP and PTCDA. However, the FT-IR spectrum of the fifth fraction possesses functional groups analogous to PTCDA moieties. Table S8† summarizes the ATR-IR peaks corresponding to the precursor, solvent, ML-1 and the fifth fraction.

The elemental composition and hybridization status of fifth fraction CDs can be determined *via* XPS analysis. The survey spectrum provides an entire scan of elements in terms of binding energy from 63.6 eV to 1200 eV (Fig. 5e). The peaks positioned at 285, 399, 532 and 1072 eV correspond to C, N, O and sodium (Na), respectively. Moreover, the peaks at 990 and 746 eV correspond to auger electrons of C and O belonging to the KLL subshell. Na can be considered as impurity as it is not a constituent element of the precursor and appears due to the glass substrate. The full scan spectrum of C 1s was deconvoluted by fitting three peaks at 284.2, 285.5 and 289.8 assigned to C–C/C=C, C–O and O=C–O groups, respectively as shown in Fig. 5f. The peaks obtained after the deconvolution of O1s spectra centered at 530.7 and 532.6 eV belong to C=O and C–O groups (Fig. 5g). The elemental composition is also obtained using component ratio analysis from the XPS data, C (53.37%) and O (31.77%) being the major elements with N (4.25%) as the minor constituent.

The surface charge of CDs determines the ability to resist agglomeration. The zeta potential of CDs estimated as −19.21 mV (Fig. 5h) through DLS measurements indicates the presence of a considerable amount of negatively charged moieties and a lower amount of nitrogen containing functional groups on the surface of the CDs. The CD dispersion could be stored for 4 months without any agglomeration.

3.7. Morphological studies

A dilute dispersion of the fifth fraction under TEM enabled us to view quasi-spherical CDs (Fig. 6a) having a diameter in the range of 1–6 nm (Fig. 6b). SAED was performed along with TEM imaging over a specific region. The diffraction patterns appear in the form of bright spots and rings (Fig. 6c) which indicate the polycrystallinity of the CDs. In addition, the measured diffraction patterns confirm the results of XRD studies. A high-resolution TEM scan image (Fig. 6d) reveals CDs having lattice infringes measured as 0.24 and 0.30 nm which matches with the (100) and (002) planes of diffraction of graphitic carbon. Besides, carbon rods that are also formed along with CDs as a by-product during the synthesis process are visible in the lower magnification TEM images (Fig. 6e). Qualitative elemental analysis along with imaging (inset of Fig. 6e) was performed using TEM-EDS. Carbon is found as
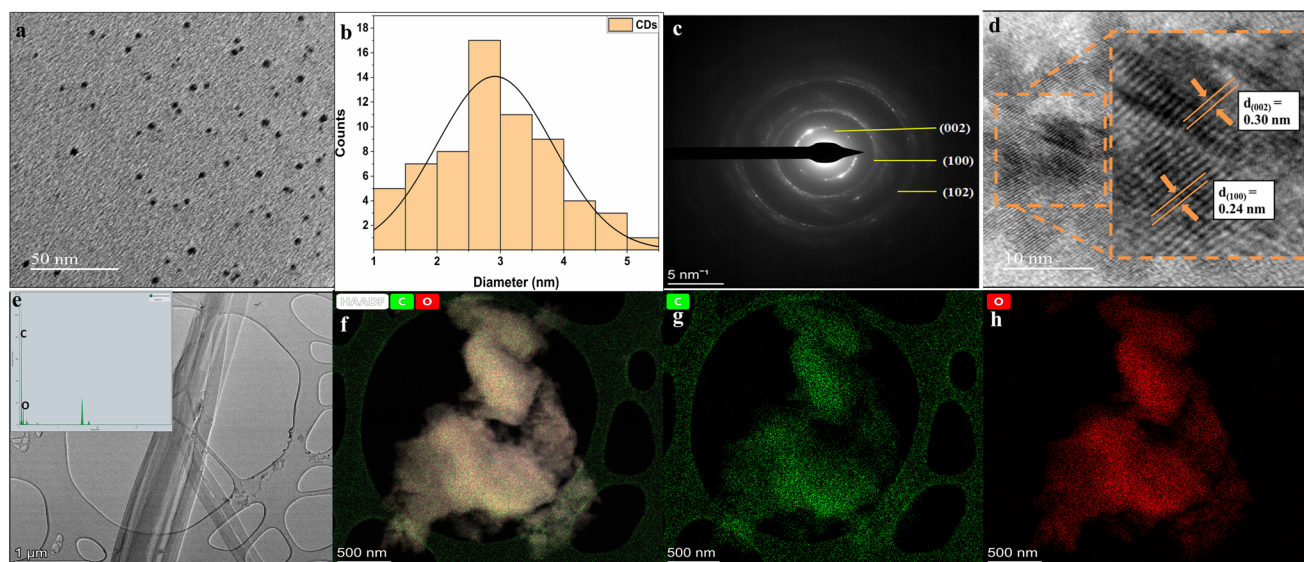

Fig. 6 (a) TEM image of CDs. (b) Size histogram of CDs having a diameter ranging between 2–4 nm. (c) SAED diffraction indicating the polycrystalline nature of CDs. (d) HRTEM image of CDs with lattice infringe. (e) TEM image depicting the presence of carbon nanorods. TEM-EDS (inset image) showing the elemental composition. (f) HAADF image with different elemental distributions and individual elemental mapping of (g) carbon and (h) oxygen.

the major element followed by O, while N is present in the minor composition. Elemental mapping further confirms the composition with carbon and oxygen as highly populated elements (Fig. 6f–h).

3.8. Fluorescence properties of CDs in the solid state

Though CDs in the liquid state display emissions at 540, 577 and 630 nm for different excitations at 455, 487 and 523 nm, the emission characteristics may differ in the solid state. Hence, CD dispersion was coated on UV dull paper and fluorescence spectra were recorded. The UV dull paper (control) exhibited major emissions at 440 and 532 nm for excitation at 370 nm (Fig. 7a). The CD coated paper sample exhibited additional peaks at 540 and 585 nm for the same excitation (Fig. 7b and c), which belong to the CDs. Besides, the emissions arising from the paper are masked by excitation at 460, 500 and 530 nm, which fascinatingly demonstrate analogous emissions at 540, 585 and 640 nm. To support these findings, the same excitations were also used on the UV dull paper and as expected they did not show any emission beyond 530 nm, further validating the results. Thus, it can be noted that there is minimal change in the emission wavelengths of CDs in the solid state.

Furthermore, the fluorescence lifetime of the CD coated paper samples was recorded for excitations at 460, 500 and

520 nm (Fig. 7d–f). The CDs in the liquid state exhibit a constant lifetime value independent of excitation as mentioned in the earlier section. Although the CDs on the paper sample exhibit mono-exponential decay (λ_{em} = 540 and 590 nm) with insignificant decline in lifetime values indicative of resonance energy transfer prevalent in solid samples; in the case of emitters corresponding to 640 nm a significant decline in fluorescence lifetime with bi-exponential decay is observed. A better fit for the bi-exponential decay plot is acquired using the equation, $I_{(t)} = A_1 \cdot e^{(-t/\tau_1)} + A_2 \cdot e^{(-t/\tau_2)}$, where $I_{(t)}$ represents the intensity of decay at the recorded time t, A_1 and A_2 correspond to amplitude fitting constants and τ_1 and τ_2 represent individual lifetime values.[47] To obtain the average lifetime value (τ_{avg}) using two lifetime values (τ_1 and τ_2) and pre-exponential factors (A_1 and A_2) the following expression $\tau_{avg} = A_1\tau_1^2 + A_2\tau_2^2 / A_1\tau_1 + A_2\tau_2$ is applied. The CDs (λ_{em} = 640 nm) coated on paper exhibit two lifetime values indicative of two different de-excitation pathways. We observe that τ_1 for all excitations (460, 500 and 520 nm) show faster decay in comparison to τ_2 with longer decay. Generally, the average lifetimes (τ_{avg}) are weakly dependent on the excitation used and greatly depend on the individual time constants.[48] Therefore CDs (λ_{em} = 640 nm) appear to undergo quenching to a greater extent in comparison to other emitting species (λ_{em} = 540 nm and λ_{em} =
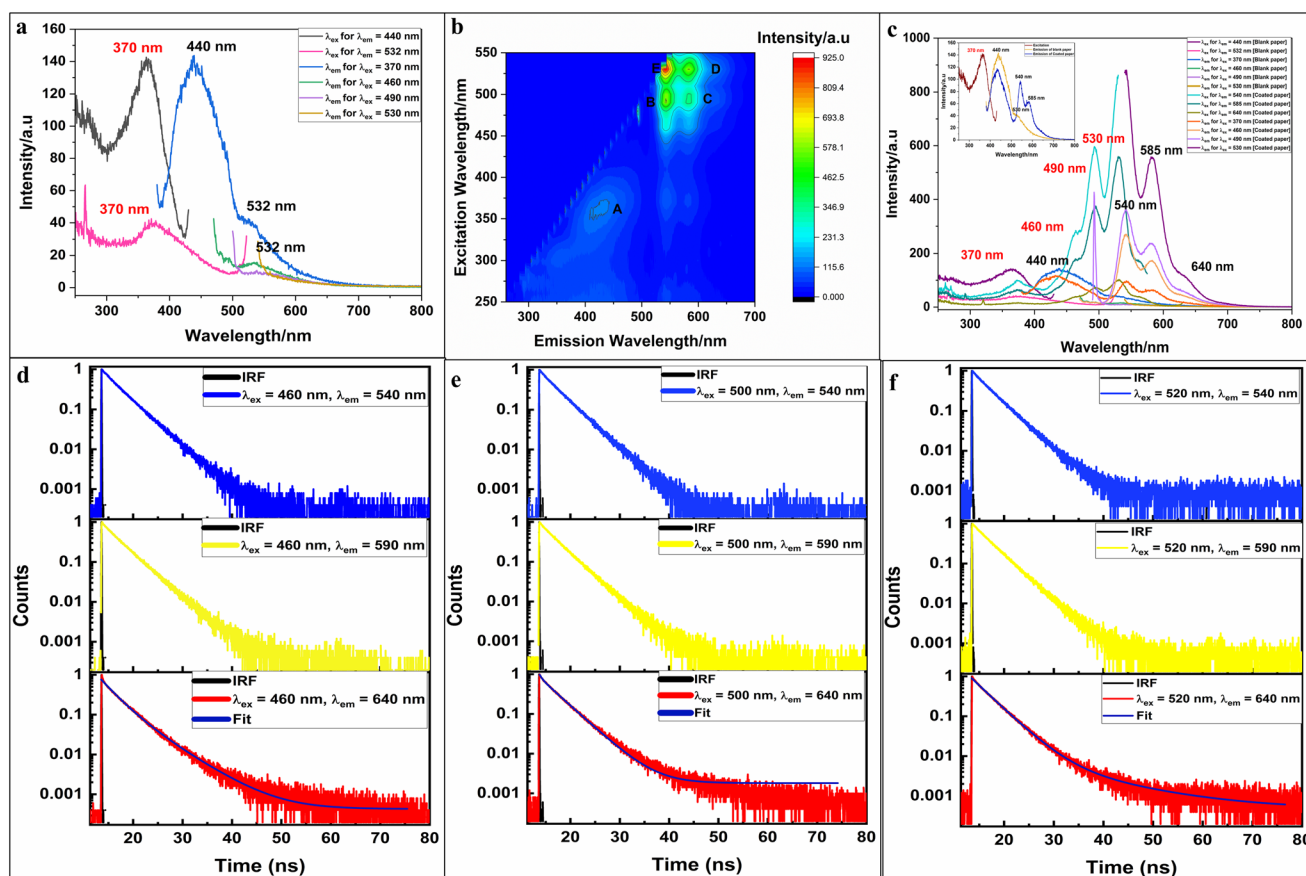

Fig. 7 (a) Fluorescence spectrum of UV dull paper. (b) 3D and (c) 2D fluorescence spectra of the CD coated paper sample. Time-resolved fluorescence spectra of the CD coated paper sample recorded under (d) 460, (e) 500 and (f) 520 nm excitation.

590 nm). The emissions centered at 540 and 590 nm are stable in the solid state. The individual lifetime value along with the average lifetime values of CDs coated on UV dull paper corresponding to different excitations and emissions are listed in Table S9.†

3.9. Ink formulation using the CDs

A flexo-ink was formulated using PVA as the binder as it enables us to achieve the desired viscosity and serves as a binder due to good adhesion and film-forming features upon drying.[58] PVA granules were added to de-ionized water and heated at 90 °C along with continuous stirring. The viscous PVA melt obtained was allowed to cool at room temperature. Furthermore, an ink was formulated by dispersing the CDs in PVA and a 30% glycerol–ethanol mixture which serves as a co/solvent. A few drops of ammonia were added to adjust the desired pH of 9 for the formulation. The ink appears pale yellow under daylight, while it exhibits bright yellow fluorescence under 365 nm UV illumination (Fig. S14a and b†). The fluorescence spectra of both the control (without CDs) and ink formulation are collected as depicted in Fig. S15a–d.† A 3D plot of the control displays spectral regions ranging between 370–532 nm (Fig. S15a†). The 2D spectra of the control formulation have emissions centered at 440 and 532 nm for excitation at 370 nm (Fig. S15b†). The spectral region for the ink lies between 460–630 nm wherein the emission from the control remains masked (Fig. S15c†). Similarly, the 2D spectra of the ink obtained showed emission peaks at 540 and 580 nm for excitations corresponding to 460, 490 and 520 nm (Fig. S15d†). The presence of CDs induces changes in the formulation to exhibit emissions in the visible region and can be therefore utilized for printing purposes.

3.10. Analysis of printing properties

The inkjet printing technique is utilized to print CDs on paper and flexible substrates. Deng and group utilized CDs synthesized *via* the solvothermal approach for ʟ-ascorbic acid in inkjet ink formulation. The letter inscribed on bond paper appeared fluorescent blue under a UV source.[59] Another report stated the use of plant dye-based CDs in inkjet formulation. A specific pattern was printed on cotton cloth which was invisible under daylight but showed distinct fluorescence under UV illumination.[60] Li *et al.* synthesized trichromatic CDs and incorporated them in an inkjet formulation.[61] Specific information can be inscribed on PVA film *via* inkjet printing to store crucial information. The prints on PVA appeared fluorescent blue, green, and red under a UV source. As CDs are more prone to undergo aggregation-induced quenching in the solid state,[62–64] they can be dispersed in salt or a polymeric matrix. The present work focuses on the suspension of CDs in a PVA matrix and the preparation of standardized flexo formulation. The flexo-ink was printed *via* the flexography technique and the print proofs obtained were assessed for photostability and abrasion resistance for real time application.

Initially drawdown of the ink was done to achieve a coating on UV dull paper. The coated sample appears as a pale pink patch under daylight and exhibits yellow fluorescence under 365 nm UV light (Fig. S16a and b†). The 2D spectrum (Fig. S16c†) for the control ink (without CDs) printed sample shows major emission at 435 nm, partly contributed by the UV dull paper. The fluorescence spectra obtained for the coated paper show distinct peaks at 540, 585 and 640 nm irrespective of different excitations (Fig. S16d†). The control exhibits emissions confined between 370–530 nm indicating that the emission peaks lying in the visible region (540, 585 and 640 nm) are due to the CDs. Furthermore, the ink was printed on the UV dull paper using the flexography technique. The emission behaviour exhibited by the printed proofs is analogous to that of the coated paper as depicted in Fig. 8a.

To assess the photostability, the printed samples of (1.0 cm × 1.0 cm) were placed under intense UV light at the rate of 300 W/30 m min^{-1} in a UV curing unit for 10, 20, 30 and 40 exposure cycles. The emission plots obtained for the printed sample subjected to different exposure cycles were monitored at inherent excitations of 370, 460, 500 and 530 nm (Fig. 8b and c). The unexposed (zero pass) and UV-exposed (10, 20, 30 & 40 passes) samples have similar emission peaks centred at 540, 585 and 640 nm but the difference lies in the relative emission intensities. When the samples are exposed to 370 nm excitation, emissions are also observed from the blank paper at 440 nm. As the region of interest lies beyond 530 nm where the emissions are due to the CDs, peak intensities at 540, 585 and 640 nm are studied. The printed samples after UV irradiation underwent a certain degree of fluorescence loss when compared with the unexposed/zero pass sample. Moreover, the emissions at 640 nm are more affected by UV exposure indicating that emitters corresponding to 540 and 585 nm tolerate a certain degree of photo-bleaching. Although the print is prone to minimal degree of photo-bleaching, there is no deteriorating effect on the print. Moreover, the coated and printed paper samples stored under ambient conditions displayed minimal changes in the emission intensity indicating good stability over a period of 5 months (Fig. S17a–f†).

The International Commission on Illumination states the utilization of 3D CIELAB colour spaces where the colours perceived by the human eye is imitated. The parameters used are L^* with values lying in the range of 0–100 which describes the whiteness of the sample as well as a^* and b^* components of the colour space which have values from −120 to 120. The positive and negative values of a^* indicate the red and green colour of the sample, whereas the positive and negative b^* values represent yellow and blue colours. In addition to these parameters, ΔE provides insight into the colour perceived by the naked eye. The print is invisible if the value is 0–2 and requires the assistance of a colour specialist, whereas the print can be deciphered by the human eye if the value of ΔE is greater than 3. L^*, a^*, b^* and density of the UV dull paper are 91.79, −0.64, 4.85 and 0.13, respectively, whereas the measured values of the printed sample are 88.6, 1.2 and 3.8. The slightly lower L^* value indicates yellowing of the print, while the positive a^* and b^* values signify reddening and yellowing of the printed sample. In the case of UV-exposed print samples, there
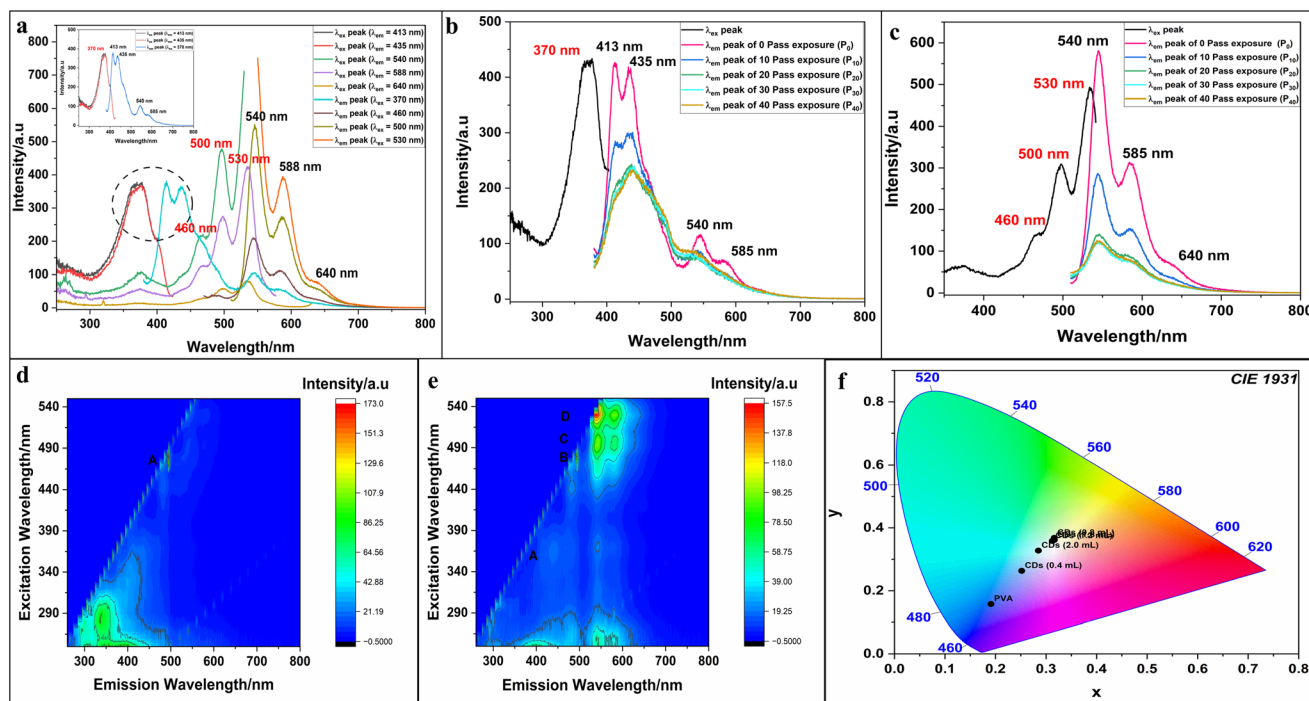
Fig. 8 (a) Photoluminescence spectra of the Flexo-printed sample recorded under different excitations. Fluorescence spectra of the UV-exposed print at (b) 370 nm and (c) 460, 500 and 530 nm. 3D photoluminescence spectra of (d) PVA and (e) composite films. (f) CIE plots for PVA and composite films with varying CD compositions under 370 nm excitation.

is no significant changes in $L*$ values while the $a*$ value shifts to a negative scale indicating a shift to green colour, whereas the $b*$ value becomes more positive indicating yellowing upon exposure to a greater number of exposure cycles. Table S10 and Fig. S18a† present the $L*$, $a*$, $b*$ and density values and graphical presentation of the blank, printed, and UV-exposed samples.

The adhesion of ink to paper is checked *via* the abrasion test wherein a print is attached to the basal stand and subjected to mechanical brushing using a rubber block for a certain duration. In this experiment, a weight block of 2 lbs was placed on the rubber pad and subjected to 50 and 100 rubs. After each stroke the color parameters and density of the prints are evaluated and are depicted in Table S11† and graphically presented in Fig. S18b.† The $L*$ values of the rub-tested samples are closer to 100 implying whiteness of the sample, which might be due to the removal of few layers of the ink film. The positive values of $a*$ and $b*$ indicate redness and yellowness of the abrasion tested samples.

3.11. CDs in composite film and security ink for flexible packaging

Food packaging mainly involves the use of synthetic plastic materials derived from petroleum products and their increasing use poses serious environmental concerns. PVA, approved by the FDA for use in clinical trials is utilised as an additive in coatings due to their ability to form an oxygen barrier, enhanced film-forming ability and attractive mechanical pro-

perties.[65] The incorporation of fluorescent CDs in PVA can facilitate the fabrication of functional composites with luminescence features.[66,67] Though emission properties can be realised in the liquid state, these nanomaterials suffer from fluorescence reduction in the solid state due to aggregation-induced quenching. However, the aggregation leads to excessive resonance transfer and can be avoided by incorporation into solid matrices like silicone, PVP or epoxy resin.[68–71] CDs with high fluorescence QYs are desirable and hence PTCDA-derived CDs were used to prepare PVA–CD composite films. CD solutions of varying volumes were dispersed in 30% PVA (10 mL) to prepare five different films. As shown in Fig. S19,† the PVA film appears translucent under daylight and exhibits blue fluorescence under UV illumination. Interestingly, the transparent composite films exhibit yellow fluorescence under UV light. The 3D fluorescence spectra of the PVA film as depicted in Fig. 8d have the spectral region confined at 450–500 nm (region marked as A). The 3D spectra of the PVA–CD composite film (Fig. 8e) exhibit their characteristic emissions at 540, 580 and 640 nm upon excitation at 370 nm (marked as A), 460 nm (marked as B), 490 nm (marked as C) and 520 nm (marked as D). The effect of varying the concentration of CDs on the fluorescent films is also analysed *via* fluorescence measurements. Fig. S20a–d† show the emission peak corresponding to the composite film with 0.8 mL CDs. The CIE plots for the films were obtained for excitation at 370 nm as depicted in Fig. 8f. Interestingly, the colour coordinates of the composite films (0.8 mL, 1.2 mL and 1.6 mL CDs)

at (0.3157, 0.3679), (0.3123, 0.3586) and (0.3162, 0.3616) correspond to white colour (encircled region). The production of white light can be realised by mixing blue and yellow emissive species and these films could be used in the fabrication of white LEDs, which may be explored further. The composite films could also be used as flexible packaging materials. Moreover, target marker-based sorting of smart packaging polymer materials could facilitate plastic waste management practices to meet high recycling rates.[72] The fluorescent CDs could also serve as fluorescent marker materials for identification of post-consumer plastic packaging for a circular economy.

The security printing applications of the PVA-based CD ink in different commercially available packaging materials such as PET films, PVC sheets, FBB boards and metalized boards are explored. Using the Flexo proofing technique, multiple coats (1×, 2× and 3×) of the ink showed good adherence to PVC sheets and FBB boards. Under daylight the print appears pale pink. However, due to the presence of certain brighteners in substrates they appear bright blue fluorescent. The authenticity of the proofs can be checked using UV block filters by the user to observe fluorescent yellow prints on PVC sheets and FBB cardboards. Furthermore, the emission profiles for the PVC print proofs (Fig. S21a–c†) exhibit prominent peaks at 540 and 580 nm (λ_{ex} = 370 and 500 nm excitations) while the peak at 440 nm belongs to PVC sheets. The FBB printed board also shows similar emissions (Fig. S21e and f†) at 540 and 580 nm (λ_{ex} = 500 excitation), while emission at 440 nm belongs to the FBB board (Fig. S21d†). The ability of the ink film to combat peeling was also evaluated for both PVC and FBB printed samples (Fig. S22a–f†). The ink printed on both the substrates demonstrates stability up to 50 rubs and an additional mechanical force induces a decline in intensity. The colorimetric values and density for both the printed substrates were also estimated as shown in Fig. S23a, b and Tables S12, 13.† The printed PVC sheet exhibited an $L*$ value closer to 100 indicating the whiteness of the sample. The positive and negative values of $a*$ and $b*$ indicated red and blue colours of the printed PVC sheet. The printed FBB boards too exhibited an $L*$ value closer to 100 with proximity towards white colour. Based on positive and negative values of $a*$ and $b*$ the printed boards showed red and blue colours. The minimal changes in colour parameters and density in printed PVC and FBB substrates (for 100 rubs) indicated resistance to peeling (Fig. S23c, d and Tables S14, 15†) of ink film. Therefore, this ink can be printed in flexible substrates exhibiting a security feature and desired stability towards scuffling. The print appears pale pink under daylight but under a UV source yellow fluorescence is evident. The uniqueness lies in the difficulty for the counterfeit to replicate similar features.

4. Conclusion

Yellow emissive CDs were synthesized using a solvothermal approach from perylene tetracarboxylate dianhydride and sep-

arated using column chromatography. Efficient purification was evidenced through superior fluorescence features of the resultant fifth fraction of interest with a QY as high as 53.22% compared to the precursor (3.76%) and mother liquor (9.78%). Moreover, the time-resolved fluorescence spectra of the fifth fraction exhibited an excitation independent lifetime value with mono-exponential decay indicating the presence of single emissive centres on the surface of the CDs. The ink formulation prepared using these fluorescent CDs and printed on UV dull paper *via* the flexography technique exhibited yellow fluorescence under UV illumination which can be used for security printing application. The ink could be used in smart packaging as the ink film deposited on PVC sheets and FBB boards exhibited good stability against scuffing, suggesting its use in the packaging industry. Moreover, the CDs when incorporated into the PVA matrix exhibited different emissions, and the corresponding colour interpretation can be decoded *via* CIE colour space plots. The CDs could also serve as fluorescent markers for further identification of post-consumer plastic packaging for a circular economy. The CD–PVA composite films have colour coordinates close to white colour for excitation at 370 nm. Hence, these composite films could also serve as functional materials for fabrication of white LEDs.

Author contributions

Namratha Ullal: data curation, formal analysis, investigation, methodology, validation, and writing – original draft. Bibekananda Sahoo: data curation, investigation, and validation. Dhanya Sunil: conceptualization, methodology, project administration, supervision, and writing – review & editing. Suresh D. Kulkarni: conceptualization, methodology, project administration, supervision, and writing – review & editing. Udaya Bhat K.: methodology, project administration, and writing – review & editing. Anand P. J.: methodology, supervision, and project administration.

Data availability

The data supporting this article have been included as part of the ESI.† The datasets generated during and/or analysed during the current study are available from the first author on reasonable request.

Conflicts of interest

There are no conflicts to declare.

Acknowledgements

DAMP (Department of Atomic and Molecular Physics), Manipal; Manipal Technologies Limited, Manipal; Central Instrumentation Facility (CIF), IISER-Thiruvananthapuram; Sophisticated Analytical Instrument Facility (SAIF), IIT-Bombay; Central Research Facility (CRF), CeNs (Centre For Nano and Soft Matter Sciences).

References

1 L. Pan, S. Sun, A. Zhang, K. Jiang, L. Zhang, C. Dong, Q. Huang, A. Wu and H. Lin, Truly Fluorescent Excitation-Dependent Carbon Dots and Their Applications in Multicolor Cellular Imaging and Multidimensional Sensing, *Adv. Mater.*, 2015, **27**(47), 7782–7787, DOI: **10.1002/ADMA.201503821**.

2 J. He, Y. He, Y. Chen, B. Lei, J. Zhuang, Y. Xiao, Y. Liang, M. Zheng, H. Zhang and Y. Liu, Solid-State Carbon Dots with Red Fluorescence and Efficient Construction of Dual-Fluorescence Morphologies, *Small*, 2017, **13**, 1700075, DOI: **10.1002/SMLL.201700075**.

3 J. Shi, G. Ni, J. Tu, X. Jin and J. Peng, Green synthesis of fluorescent carbon dots for sensitive detection of Fe^{2+} and hydrogen peroxide, *J. Nanopart. Res.*, 2017, **19**, 1–10, DOI: **10.1007/S11051-017-3888-5/FIGURES/10**.

4 C. Rizzo, F. Arcudi, L. Đorđević, N. T. Dintcheva, R. Noto, F. D'Anna and M. Prato, Nitrogen-Doped Carbon Nanodots-Ionogels: Preparation, Characterization, and Radical Scavenging Activity, *ACS Nano*, 2018, **12**, 1296–1305, DOI: **10.1021/ACSNANO.7B07529/SUPPL_FILE/NN7B07529_SI_001.PDF**.

5 X. Xu, R. Ray, Y. Gu, H. J. Ploehn, L. Gearheart, K. Raker and W. A. Scrivens, Electrophoretic analysis and purification of fluorescent single-walled carbon nanotube fragments, *J. Am. Chem. Soc.*, 2004, **126**, 12736–12737, DOI: **10.1021/JA040082H/SUPPL_FILE/JA040082H_S.PDF**.

6 S. T. Yang, L. Cao, P. G. Luo, F. Lu, X. Wang, H. Wang, M. J. Meziani, Y. Liu, G. Qi and Y. P. Sun, Carbon dots for optical imaging in vivo, *J. Am. Chem. Soc.*, 2009, **131**, 11308–11309, DOI: **10.1021/JA904843X/SUPPL_FILE/JA904843X_SI_001.PDF**.

7 W. Su, H. Wu, H. Xu, Y. Zhang, Y. Li, X. Li and L. Fan, Carbon dots: a booming material for biomedical applications, *Mater. Chem. Front.*, 2020, **4**, 821–836, DOI: **10.1039/C9QM00658C**.

8 P. Das, M. Bose, A. K. Das, S. Banerjee and N. C. Das, One-Step Synthesis of Fluorescent Carbon Dots for Bio-Labeling Assay, *Macromol. Symp.*, 2018, **382**, 1800077, DOI: **10.1002/MASY.201800077**.

9 H. Barhum, T. Alon, M. Attrash, A. Machnev, I. Shishkin and P. Ginzburg, Multicolor Phenylenediamine Carbon Dots for Metal-Ion Detection with Picomolar Sensitivity, *ACS Appl. Nano Mater.*, 2021, **4**, 9919–9931, DOI: **10.1021/ACSANM.1C02496/ASSET/IMAGES/LARGE/AN1C02496_0010.JPEG**.

10 X. J. Xu, S. Ge, D. Q. Li, Z. Q. Xu, E. J. Wang and S. M. Wang, Fluorescent carbon dots for sensing metal ions and small molecules, *Chin. J. Anal. Chem.*, 2022, **50**, 103–111, DOI: **10.1016/J.CJAC.2021.09.005**.

11 G. Calabrese, G. D. Luca, G. Nocito, M. G. Rizzo, S. P. Lombardo, G. Chisari, S. Forte, E. L. Sciuto and S. Conoci, Carbon Dots: An Innovative Tool for Drug Delivery in Brain Tumors, *Int. J. Mol. Sci.*, 2021, **22**, 11783, DOI: **10.3390/IJMS222111783**.

12 Z. X. Wang, Z. Wang and F. G. Wu, Carbon Dots as Drug Delivery Vehicles for Antimicrobial Applications: A Minireview, *ChemMedChem*, 2022, **17**, e202200003, DOI: **10.1002/CMDC.202200003**.

13 Y. C. Liang, S. S. Gou, K. K. Liu, W. J. Wu, C. Z. Guo, S. Y. Lu, J. H. Zang, X. Y. Wu, Q. Lou, L. Dong, Y. F. Gao and C. X. Shan, Ultralong and efficient phosphorescence from silica confined carbon nanodots in aqueous solution, *Nano Today*, 2020, **34**, 100900, DOI: **10.1016/J.NANTOD.2020.100900**.

14 X. Li, M. Rui, J. Song, Z. Shen and H. Zeng, Carbon and Graphene Quantum Dots for Optoelectronic and Energy Devices, A Review, *Adv. Funct. Mater.*, 2015, **25**, 4929–4947, DOI: **10.1002/ADFM.201501250**.

15 Y. Yao, H. Zhang, K. Hu, G. Nie, Y. Yang, Y. Wang, X. Duan and S. Wang, Carbon dots based photocatalysis for environmental applications, *J. Environ. Chem. Eng.*, 2022, **10**, 107336, DOI: **10.1016/J.JECE.2022.107336**.

16 K. Akbar, E. Moretti and A. Vomiero, Carbon Dots for Photocatalytic Degradation of Aqueous Pollutants: Recent Advancements, *Adv. Opt. Mater.*, 2021, **9**, 2100532, DOI: **10.1002/ADOM.202100532**.

17 Y. Wang and A. Hu, Carbon quantum dots: Synthesis, properties and applications, *J. Mater. Chem. C*, 2014, **2**, 6921–6939, DOI: **10.1039/c4tc00988f**.

18 A. Mikhraliieva, V. Zaitsev, R. Q. Aucélio, H. B. Da Motta and M. Nazarkovsky, Benefit of porous silica nanoreactor in preparation of fluorescence carbon dots from citric acid, *Nano Express*, 2020, **1**, DOI: **10.1088/2632-959X/ab7e0d**.

19 W. U. Khan, D. Wang, W. Zhang, Z. Tang, X. Ma, X. Ding, S. Du and Y. Wang, High Quantum Yield Green-Emitting Carbon Dots for Fe(III) Detection, Biocompatible Fluorescent Ink and Cellular Imaging, *Sci. Rep.*, 2017, **7**, 1–9, DOI: **10.1038/s41598-017-15054-9**.

20 C. Y. Chang, S. Venkatesan, A. Herman, C. Lo Wang, H. Teng and Y. L. Lee, Carbon quantum dots with high quantum yield prepared by heterogeneous nucleation processes, *J. Alloys Compd.*, 2023, **938**, 168654, DOI: **10.1016/J.JALLCOM.2022.168654**.

21 A. Sharma and J. Das, Small molecules derived carbon dots: synthesis and applications in sensing, catalysis, imaging, and biomedicine, *J. Nanobiotechnol.*, 2019, **17**, 1–24, DOI: **10.1186/S12951-019-0525-8**.

22 R. Atchudan, S. C. Kishore, P. Gangadaran, T. N. J. I. Edison, S. Perumal, R. L. Rajendran, M. Alagan, S. Al-Rashed, B. C. Ahn and Y. R. Lee, Tunable fluorescent carbon dots from biowaste as fluorescence ink and imaging human normal and cancer cells, *Environ. Res.*, 2022, **204**, 112365, DOI: **10.1016/J.ENVRES.2021.112365**.

23 S. Chahal, J. R. Macairan, N. Yousefi, N. Tufenkji and R. Naccache, Green synthesis of carbon dots and their applications, *RSC Adv.*, 2021, **11**, 25354–25363, DOI: **10.1039/D1RA04718C**.

24 J. Wang, C. F. Wang and S. Chen, Amphiphilic Egg-Derived Carbon Dots: Rapid Plasma Fabrication, Pyrolysis Process, and Multicolor Printing Patterns, *Angew. Chem., Int. Ed.*, 2012, **51**, 9297–9301, DOI: **10.1002/ANIE.201204381**.

25 Q. Wang, X. Liu, L. Zhang and Y. Lv, Microwave-assisted synthesis of carbon nanodots through an eggshell membrane and their fluorescent application, *Analyst*, 2012, **137**, 5392–5397, DOI: **10.1039/C2AN36059D**.

26 W. Lu, X. Qin, S. Liu, G. Chang, Y. Zhang, Y. Luo, A. M. Asiri and A. O. Al-Y, Xuping Sun, Economical, green synthesis of fluorescent carbon nanoparticles and their use as probes for sensitive and selective detection of mercury (II) ions, *Anal. Chem.*, 2012, **84**, 5351–5357, DOI: **10.1021/ac3007939**.

27 R. Atchudan, T. N. J. I. Edison, K. R. Aseer, S. Perumal, N. Karthik and Y. R. Lee, Highly fluorescent nitrogen-doped carbon dots derived from Phyllanthus acidus utilized as a fluorescent probe for label-free selective detection of Fe^{3+} ions, live cell imaging and fluorescent ink, *Biosens. Bioelectron.*, 2018, **99**, 303–311, DOI: **10.1016/j.bios.2017.07.076**.

28 R. Atchudan, T. N. J. I. Edison, S. Perumal, R. Vinodh and Y. R. Lee, Betel-derived nitrogen-doped multicolor carbon dots for environmental and biological applications, *J. Mol. Liq.*, 2019, **296**, 111817, DOI: **10.1016/j.molliq.2019.111817**.

29 P. Krishnaiah, R. Atchudan, S. Perumal, E. S. Salama, Y. R. Lee and B. H. Jeon, Utilization of waste biomass of Poa pratensis for green synthesis of n-doped carbon dots and its application in detection of Mn^{2+} and Fe^{3+}, *Chemosphere*, 2022, **286**, 131764, DOI: **10.1016/j.chemosphere.2021.131764**.

30 R. Atchudan, T. N. J. I. Edison, D. Chakradhar, S. Perumal, J. J. Shim and Y. R. Lee, Facile green synthesis of nitrogen-doped carbon dots using Chionanthus retusus fruit extract and investigation of their suitability for metal ion sensing and biological applications, *Sens. Actuators, B*, 2017, **246**, 497–509, DOI: **10.1016/j.snb.2017.02.119**.

31 M. Zheng, Y. Li, S. Liu, W. Wang, Z. Xie and X. Jing, One-Pot to Synthesize Multifunctional Carbon Dots for Near Infrared Fluorescence Imaging and Photothermal Cancer Therapy, *ACS Appl. Mater. Interfaces*, 2016, **8**, 23533–23541, DOI: **10.1021/ACSAMI.6B07453/ASSET/IMAGES/LARGE/AM-2016-07453X_0006.JPEG**.

32 W. Gao, H. Song, X. Wang, X. Liu, X. Pang, Y. Zhou, B. Gao and X. Peng, Carbon Dots with Red Emission for Sensing of Pt2+, Au3+, and Pd2 + and Their Bioapplications in Vitro and in Vivo, *ACS Appl. Mater. Interfaces*, 2018, **10**, 1147–1154, DOI: **10.1021/ACSAMI.7B16991/ASSET/IMAGES/LARGE/AM-2017-169912_0002.JPEG**.

33 J. F. Li, X. Y. Ma and M. L. Ma, Preparation and performance study of dye-based carbon quantum dots, *Inorg. Chem. Commun.*, 2023, **150**, 110541, DOI: **10.1016/j.inoche.2023.110541**.

34 F. Würthner, C. R. Saha-Möller, B. Fimmel, S. Ogi, P. Leowanawat and D. Schmidt, Perylene Bisimide Dye Assemblies as Archetype Functional Supramolecular Materials, *Chem. Rev.*, 2016, **116**, 962–1052, DOI: **10.1021/acs.chemrev.5b00188**.

35 H. Z. Wang, L. G. Ning, W. Y. Lv, L. Xiao, C. M. Li, Z. S. Lu, B. Wang and L. Q. Xu, Green synthesis of perylene diimide-based nanodots for carbon dioxide sensing, antibacterial activity prediction and bacterial discrimination, *Dyes Pigm.*, 2020, **176**, 108245, DOI: **10.1016/j.dyepig.2020.108245**.

36 M. Moniruzzaman, S. D. Dutta, K. T. Lim and J. Kim, Perylene-Derived Hydrophilic Carbon Dots with Polychromatic Emissions as Superior Bioimaging and NIR-Responsive Photothermal Bactericidal Agent, *ACS Omega*, 2022, **7**, 37388–37400, DOI: **10.1021/acsomega.2c04130**.

37 K. Y. Chen and C. W. Chang, Highly soluble monoamino-substituted perylene tetracarboxylic dianhydrides: Synthesis, optical and electrochemical properties, *Int. J. Mol. Sci.*, 2014, **15**, 22642–22660, DOI: **10.3390/ijms151222642**.

38 Y. J. Ou, X. M. Wang, C. L. Li, Y. L. Zhu and X. L. Li, The Effects of Alkali and Temperature on the Hydrolysis Rate of N-methylpyrrolidone, in *IOP Conference Series: Earth and Environmental Science*, Institute of Physics Publishing, 2017. DOI: **10.1088/1755-1315/100/1/012036**.

39 V. V. Semenov, N. V. Zolotareva, E. Yu. Ladilina, S. A. Lermontova, L. G. Klapshina, I. S. Grigor'ev, M. A. Lopatin, A. I. Kirillov, T. I. Kulikova and G. A. Domrachev, Reaction of perylene-3,4,9,10-tetracarboxylic acid dianhydride with 3-aminopropyltriethoxysilane and hexamethyldisilazane, *Russ. J. Gen. Chem.*, 2011, **81**, 1496–1506, DOI: **10.1134/S1070363211070152/METRICS**.

40 G. Song, Y. Lin, Z. Zhu, H. Zheng, J. Qiao, C. He and H. Wang, Strong fluorescence of poly (N-vinylpyrrolidone) and its oxidized hydrolyzate, *Macromol. Rapid Commun.*, 2015, **36**, 278–285, DOI: **10.1002/marc.201400516**.

41 S. Khan, A. Gupta, N. C. Verma and C. K. Nandi, Time-Resolved Emission Reveals Ensemble of Emissive States as the Origin of Multicolor Fluorescence in Carbon Dots, *Nano Lett.*, 2015, **15**, 8300–8305, DOI: **10.1021/acs.nanolett.5b03915**.

42 J. R. Lakowicz, *Principles of fluorescence spectroscopy*, Springer, 2006.

43 A. Das, V. Gude, D. Roy, T. Chatterjee, C. K. De and P. K. Mandal, On the Molecular Origin of Photoluminescence of Nonblinking Carbon Dot, *J. Phys. Chem. C*, 2017, **121**, 9634–9641, DOI: **10.1021/ACS.JPCC.7B02433**.

44 G. Minervini, A. Panniello, A. Madonia, C. M. Carbonaro, F. Mocci, T. Sibillano, C. Giannini, R. Comparelli, C. Ingrosso, N. Depalo, E. Fanizza, M. L. Curri and M. Striccoli, Photostable carbon dots with intense green emission in an open reactor synthesis, *Carbon*, 2022, **198**, 230–243, DOI: **10.1016/J.CARBON.2022.07.034**.

45 J. Guo, Y. Li, X. Shan, D. Wang, P. Tian and Y. Wang, Facile Microwave Synthesis of Efficient Green Emissive Carbon

Dots Powder and Their Application in Visible Light Communication and White Light Emitting Devices, *Adv. Opt. Mater.*, 2023, 2300984, DOI: **10.1002/ADOM.202300984**.

46 C. Zheng, X. An and J. Gong, Novel pH sensitive N-doped carbon dots with both long fluorescence lifetime and high quantum yield, *RSC Adv.*, 2015, **5**, 32319–32322, DOI: **10.1039/c5ra01986a**.

47 X.-H. Hu and X. An, Green synthesis of fluorescent carbon dots from ascorbic acid and their application in sensing and biological imaging, *Next Mater.*, 2024, **4**, 100226, DOI: **10.1016/j.nxmate.2024.100226**.

48 G. E. LeCroy, F. Messina, A. Sciortino, C. E. Bunker, P. Wang, K. A. S. Fernando and Y. P. Sun, Characteristic Excitation Wavelength Dependence of Fluorescence Emissions in Carbon 'quantum' Dots, *J. Phys. Chem. C*, 2017, **121**, 28180–28186, DOI: **10.1021/acs.jpcc.7b10129**.

49 H. Liu, Z. Li, Y. Sun, X. Geng, Y. Hu, H. Meng, J. Ge and L. Qu, Synthesis of Luminescent Carbon Dots with Ultrahigh Quantum Yield and Inherent Folate Receptor-Positive Cancer Cell Targetability, *Sci. Rep.*, 2018, **8**, 1086, DOI: **10.1038/s41598-018-19373-3**.

50 T. Wang, A. Wang, R. Wang, Z. Liu, Y. Sun, G. Shan, Y. Chen and Y. Liu, Carbon dots with molecular fluorescence and their application as a 'turn-off' fluorescent probe for ferricyanide detection, *Sci. Rep.*, 2019, **9**, 10723, DOI: **10.1038/s41598-019-47168-7**.

51 M. Maruthupandi, P. Varatharajan, I. B. S Banu, M. H. Mamat and N. Vasimalai, White light emitting diode and anti-counterfeiting applications of microwave assisted synthesized green fluorescent carbon dots derived from waste curry leaves, *Results Opt.*, 2022, **8**, 100249, DOI: **10.1016/J.RIO.2022.100249**.

52 D. Tenne, S. Park, T. Kampen, A. Das, R. Scholz and D. Zahn, Single crystals of the organic semiconductor perylene tetracarboxylic dianhydride studied by Raman spectroscopy, *Phys. Rev. B: Condens. Matter Mater. Phys.*, 2000, **61**, 14564–14569, DOI: **10.1103/PhysRevB.61.14564**.

53 B. Jiang, T. Huang, P. Yang, X. Xi, Y. Su, R. Liu and D. Wu, Solution-processed perylene diimide-ethylene diamine cathodes for aqueous zinc ion batteries, *J. Colloid Interface Sci.*, 2021, **598**, 36–44, DOI: **10.1016/j.jcis.2021.04.018**.

54 X. Xu, L. Xing, X. Liu, H. Du, Z. Men, Z. Dong, W. Zhang, S. Wang and C. Sun, Exploring the change of hydrogen bond evolution in NMP-H_2O solution through 2D Raman-COS spectra analysis, *J. Mol. Struct.*, 2024, **1297**, 136927, DOI: **10.1016/j.molstruc.2023.136927**.

55 P. J. Unwin, D. Onoufriou, J. J. Cox, C. P. A. Mulcahy and T. S. Jones, Interfacial chemistry of perylene-3,4,9,10-tetra-carboxylic dianhydride during the initial stages of ®lm growth on InAs(1 1 1)A, *Surf. Sci.*, 2001, **482–485**, 1210–1215, DOI: **10.1016/S0039-6028(01)00867-6**.

56 F. Kong and B. Tang, Surface-enhanced Raman scattering of graphene oxide chemically modified by perylene diimide, *Vib. Spectrosc.*, 2023, **129**, 103602, DOI: **10.1016/j.vibspec.2023.103602**.

57 E. Yakimchuk, V. Volodin and I. Antonova, New graphene derivative with: N-methylpyrrolidone: Suspension, structural, optical and electrical properties, *Phys. Chem. Chem. Phys.*, 2019, **21**, 12494–12504, DOI: **10.1039/c9cp01612k**.

58 A. Salisu, H. Abba and M. Inuwa, Preparation and Application of Polyvinyl Alcohol Based UV Curable Flexographic Printing Ink, *Int. J. Eng. Appl. Sci.*, 2015, **2**, 109–116.

59 Y. Deng, J. Qian and Y. Zhou, Solvothermal Synthesis and Inkjet Printing of Carbon Quantum Dots, *ChemistrySelect*, 2020, **5**, 14930–14934, DOI: **10.1002/slct.202003487**.

60 L. Li, Y. Han, L. Wang, W. Jiang and H. Zhao, Dye Plants Derived Carbon Dots for Flexible Secure Printing, *Nanomaterials*, 2022, **12**, 3168, DOI: **10.3390/nano12183168**.

61 J. Li, G. Xu, Y. Lu, X. Xia, W. Song, Q. Wang and C. Liu, One-Pot Synthesis of Trichromatic Fluorescent Carbon Dots for Printing and Imaging, *ACS Appl. Nano Mater.*, 2023, **6**, 10618–10625, DOI: **10.1021/acsanm.3c01556**.

62 M. Sun, S. Qu, Z. Hao, W. Ji, P. Jing, H. Zhang, L. Zhang, J. Zhaoa and D. Shen, Towards efficient solid-state photoluminescence based on carbon-nanodots and starch composites, *Nanoscale*, 2014, **6**, 13076–13081, DOI: **10.1039/c4nr04034a**.

63 Z. Xie, F. Wang and C. Y. Liu, Organic-inorganic hybrid functional carbon dot gel glasses, *Adv. Mater.*, 2012, **24**, 1716–1721, DOI: **10.1002/adma.201104962**.

64 R. Guo, T. Li and S. Shi, Electron transition pathways of graphene oxide quantum dots unraveled by emission wavelength dependent photoluminescence lifetime, *RSC Adv.*, 2017, **7**, 19701–19706, DOI: **10.1039/C7RA02365K**.

65 P. K. Panda, K. Sadeghi and J. Seo, Recent advances in poly (vinyl alcohol)/natural polymer based films for food packaging applications: A review, Food Packag, *Shelf Life*, 2022, **33**, 100904, DOI: **10.1016/j.fpsl.2022.100904**.

66 W. Yang, G. Qi, J. M. Kenny, D. Puglia and P. Ma, Effect of Cellulose Nanocrystals and Lignin Nanoparticles on Mechanical, Antioxidant and Water Vapour Barrier Properties of Glutaraldehyde Crosslinked PVA Films, *Polymers*, 2020, **12**, 1364, DOI: **10.3390/POLYM12061364**.

67 I. B. Basumatary, A. Mukherjee, V. Katiyar and S. Kumar, Biopolymer-based nanocomposite films and coatings: recent advances in shelf-life improvement of fruits and vegetables, *Crit. Rev. Food Sci. Nutr.*, 2022, **62**, 1912–1935, DOI: **10.1080/10408398.2020.1848789**.

68 Q. Han, W. Xu, C. Ji, G. Xiong, C. Shi, D. Zhang, W. Shi, Y. Jiang and Z. Peng, Multicolor and Single-Component White Light-Emitting Carbon Dots from a Single Precursor for Light-Emitting Diodes, *ACS Appl. Nano Mater.*, 2022, **5**, 15914–15924, DOI: **10.1021/acsanm.2c04130**.

69 W. Cai, T. Zhang, M. Xu, M. Zhang, Y. Guo, L. Zhang, J. Street, W. J. Ong and Q. Xu, Full color carbon dots through surface engineering for constructing white light-emitting diodes, *J. Mater. Chem. C*, 2019, **7**, 2212–2218, DOI: **10.1039/c9tc00274j**.

70 P. Ma, X. Sun, W. Pan, G. Yu and J. Wang, Green and Orange Emissive Carbon Dots with High Quantum Yields Dispersed in Matrices for Phosphor-Based White LEDs,

ACS Sustainable Chem. Eng., 2020, **8**, 3151–3161, DOI: **10.1021/acssuschemeng.9b06008**.

71 Z. Yan, T. Chen, L. Yan, X. Liu, J. Zheng, F. Ren, Y. Yang, B. Liu, X. Liu and B. Xu, One-Step Synthesis of White-Light-Emitting Carbon Dots for White LEDs with a High Color Rendering Index of 97, *Adv. Sci.*, 2023, **10**, 12, DOI: **10.1002/advs.202206386**.

72 J. Woidasky, I. Sander, A. Schau, J. Moesslein, P. Wendler, D. Wacker, G. Gao, D. Kirchenbauer, V. Kumar, D. Busko, I. A. Howard, B. S. Richards, A. Turshatov, S. Wiethoff and C. L. Koetz, Inorganic fluorescent marker materials for identification of post-consumer plastic packaging, *Resour., Conserv. Recycl.*, 2020, **161**, 104976, DOI: **10.1016/j. resconrec.2020.104976**.